Basin-Wavelength Equatorial Deep Jet Signals Across Three Oceans*

Madeleine K. Youngs

NOAA/Pacific Marine Environmental Laboratory, Seattle WA and Environmental Science and Engineering, California Institute of Technology, Pasadena CA

Gregory C. Johnson *

NOAA/Pacific Marine Environmental Laboratory, Seattle WA

for *Journal of Physical Oceanography*

submitted 3 September 2014

revised 1 March 2015

**Corresponding author address:* Gregory C. Johnson, NOAA/Pacific Marine Environmental Laboratory, 7600 Sand Point Way NE Bldg. 3, Seattle, WA 98115.

E-mail: gregory.c.johnson@noaa.gov

*Pacific Marine Environmental Laboratory Contribution Number 4218

ABSTRACT

Equatorial Deep Jets (EDJs) are equatorially trapped, stacked, zonal currents that reverse direction every few hundred meters in depth throughout much of the water column. This study evaluates their structure observationally in all three oceans using new high vertical resolution Argo float conductivity-temperature-depth (CTD) instrument profiles from 2010–2014 augmented with historical shipboard CTD from 1972–2014 and lower vertical resolution Argo float profiles from 2007–2014. Vertical strain of density is calculated from the profiles and analyzed in a stretched vertical coordinate system determined from the mean vertical density structure. The power spectra of vertical strain in each basin are analyzed using a wavelet decomposition. In the Indian and Pacific oceans, there are two distinct peaks in the power spectra, one Kelvin-wave-like and the other entirely consistent with the dispersion relation of a linear first-meridional-mode equatorial Rossby wave. In the Atlantic Ocean, the first-meridional-mode Rossby wave signature is very strong, and dominates. In all three ocean basins Rossby-wave-like signatures are coherent across the basin width, and appear to have wavelengths the scale of the basin width, with periods of 5 ± 1 years in the Indian and Atlantic oceans and 12 ± 5 years in the Pacific Ocean. Their observed meridional scales are about 1.5 times the linear theoretical values. Their phase propagation is downward with time, implying upward energy propagation if linear wave dynamics hold.

1. Introduction

Equatorial Deep Jets (EDJs) are equatorially trapped, stacked, zonal currents that alternate direction every few hundred meters in depth. The jets present in all three ocean basins, throughout much of the water column (Johnson et al. 2002; Johnson and Zhang 2003; Luyten and Swallow 1976). In recent years, the effects of the EDJs on water-mass-property distributions have been studied in the Atlantic Ocean. For example, Schmid et al. (2005) find that EDJs affect zonal transport of intermediate and deep water masses in the Atlantic. Brandt et al. (2011, 2012) argue that as well as ventilating the deep equatorial Atlantic Ocean, the EDJs even force inter-annual atmospheric variability through their upward energy propagation. We are not aware of similar studies in the Indian and Pacific oceans even though the equatorial Pacific strongly affects global climate on interannual and perhaps longer time-scales (e.g., Ropelewski and Jones 1987; England et al. 2014). Thus, we are motivated to study the structure and dynamics of the EDJs across all three oceans.

Many different surveys and analyses have focused on EDJs signatures on the Equator in the Pacific. In meridional velocity transects at 168°E and 179°E, dropsonde profiles recorded features with vertical scales of hundreds of meters and time scales longer than the 1-month cruise (Eriksen 1981). These data exhibit very little zonal coherence, perhaps owing to the Gilbert Islands separating the two transects. Using an equatorial transect of dropsonde profiles, Leetmaa and Spain (1981) find zonal currents of $\sim$300-m vertical scale with zonal coherence of greater than 10° of longitude. Firing (1987) uses 16 months of dropsonde measurements in meridional transects at 159°W, collected during the Line Islands Profiling Project as part of the PEQUOD campaign, to investigate these deep zonal currents. That study finds EDJs with a vertical scale of 150–400 m between the thermocline and 3000-m depth that exhibit sporadic vertical shifts in position. Ponte and Luyten (1989) perform spectral analysis on 16 months of dropsonde and CTD data collected over 20° longitude also as part of the PEQUOD campaign to study the EDJs. They see two peaks at 560 and 400–331 stretched meters and call the latter the EDJs, but have a difficult time characterizing the EDJ signal. Using historical CTD data, Johnson et al. (2002) find EDJs in the eastern Equatorial Pacific with a vertical wavelength of 400 stretched decibars and a decades-long period.

The use of unstretched and stretched vertical coordinates in various studies makes an exact comparison of wavelengths difficult, as the vertical density profiles used for the stretching would be required. However, the reported EDJ vertical wavelengths appear to be in general agreement. As long Rossby and Kelvin waves are geostrophic, their signatures in vertical strain and zonal velocity should have identical vertical wavelengths (e.g., Eriksen 1982).

Dropsonde measurements in the western Indian Ocean collected in April and June 1979 allow identification of zonal jets of 500–429 stretched meters vertical wavelength on the Equator, (Ponte and Luyten 1990), longer than that in the Pacific. Velocity and CTD profiles along 80.5°E in the Indian Ocean between December 1990 and September 1994 find EDJs with a vertical wavelength of 660 stretched meters (Dengler and Quadfasel 2002).

In the Atlantic Ocean, velocity profiles from sections along 35°W and 13°W find EDJs with a vertical scale of 400–600 meters, also larger than the vertical scale in the Pacific (Gouriou et al. 1999). Velocity profiles along 35°W, 23°W, and 10°W from summer of 1999 show coherence of EDJs over 25° longitude (Gouriou et al. 2001). Vertical strain sections from historical CTD data show a peak around 661-sdbars in the Atlantic ocean with a period of 5 ± 1 years, downward phase propagation, and a zonal wavelength of $70° \pm 60°$ longitude (Johnson and Zhang 2003). Similar period results are found from Argo float velocity data and much higher temporal resolution moored velocity profiler data (Brandt et al. 2011).

Many studies have interpreted EDJ observations in the Pacific within the framework of linear wave theory. Eriksen (1981) recognizes the need for long-period Rossby waves to explain the width of the jets, but also finds that Kelvin waves may play a role, and that short-period mixed Rossby-gravity waves may help to explain the meridional velocity on the Equator. Leetmaa and Spain (1981) suggest that the EDJs are either long Rossby or Kelvin waves. The two spectral peaks seen by Ponte and Luyten (1989) are interpreted separately. The peak at 560 stretched meters is characterized as a first-meridional-mode equatorial Rossby wave and the peak at 331–400 stretched meters is characterized as a packet of Kelvin waves. Muench et al. (1994) find that the EDJs perturb potential vorticity, a feature that is seen in equatorial Rossby, but not Kelvin waves. Johnson et al. (2002) suggest that the EDJs in the Eastern Pacific may be consistent with Kelvin wave phase relations, but without the benefit of much off-equatorial data to distinguish between Kelvin and Rossby waves. Thus, the interpretation of the EDJs in the Pacific appears ambiguous.

In the Indian Ocean, Ponte and Luyten (1990) find the component of the EDJs with vertical wavelength of 429 stretched meters to be consistent with Kelvin wave phase relations, but could not resolve the feature with 500-stretched meter vertical wavelength. On the other hand, Dengler and Quadfasel (2002) find the EDJs at 660-stretched meter vertical wavelength to be consistent with a non-dispersive first-meridional-mode Rossby wave by phase relations and meridional distributions of zonal velocity. From current meter moorings in the eastern Atlantic, Weisberg and Horigan (1981) find EDJs to be similar to long Rossby waves. Dropsonde measurements taken at 36°W are most consistent with Kelvin wave dynamics (Eriksen 1982). The meridional structure of vertical strain of the EDJs is consistent with first-meridional-mode Rossby waves, although too broad for simple inviscid theory (Johnson and Zhang 2003). Brandt et al. (2011) find maximum explained variance of the 1000-m Argo velocities for a high vertical mode westward-propagating Rossby wave signature of basin wavelength.

This study investigates the EDJs in all three ocean basins to compare and contrast their features. We use vertical strain (ξ_z), a measurement of the squashing and stretching of the density field, to analyze the EDJs. We compute vertical strain from a large quantity of historical shipboard CTD and Argo float profiles. Vertical displacement has also been used to analyze the density field (e.g., Eriksen 1982), but is strongly aliased by profile-to-profile differences in salinity calibrations (Eriksen 1981). In order to avoid these errors, which could be a very significant source of noise when using data from many different instruments and cruises, we use ξ_z instead. We use the Wentzel-Kramers-Brillouin-Jeffreys (WKBJ)-scaled stretched pressure (sdbar) as a vertical coordinate to account for the impacts of varying stratification (Leaman and Sanford 1975). We discuss the data used and their processing in Section 2. We provide a qualitative description of vertical strain sections from the Pacific in Section 3 and follow with quantitative analysis using wavelet decomposition in all three ocean basins in Section 4. In Section 5, we summarize and discuss the results.

2. Data and Processing

Here we use a mix of high vertical resolution shipboard CTD and recent Argo profiles, supplemented where necessary by lower vertical resolution Argo profiles. Traditionally, owing to a slow data telemetry system and power limitations, Argo floats sample at varying resolutions with a median of around 70 samples per 2000-m profile. Vertical sample spacing for these floats generally increases with increasing depth. Starting in 2006, Argo floats that report data at a vertical resolution of 2 dbars began to be incorporated into the global network, with many of these floats deployed in the equatorial Pacific beginning in 2010. This increased sampling resolution is made possible by the use of the Iridium satellite for communication. Compared to the Argo profiles, the shipboard CTD stations available are quite sparse in space, but owing to their longer historical record, as well as the fact that they sometimes extend to the ocean bottom, they are included in analysis (Figure 1). Shipboard CTD data were assembled from the National Oceanographic Data Center (NODC), Pacific Marine Environmental Laboratory (PMEL), and CLIVAR & Carbon Hydrographic Data Office (CCHDO) databases.

We find 7,113 Argo profiles within $\pm 8.5°$ latitude of the Equator across the Pacific Ocean dating from January 2010 through May 2014 that reach at least 1990-dbar pressure with no data gaps larger than 20 dbar (Figure 1, Table 1). These profiles are only from Argo floats using Iridium telecommunications. We add to those data profiles from 2,863 shipboard CTD stations reaching at least 1990 dbars and containing no data gaps of greater than 20 dbars within $\pm 8.5°$ of the Equator across the Pacific (Figure 1) for the years 1974 to 2012, after carefully screening for and eliminating any possible duplicate stations. Data are sparse from 1972–1984, so these years are not plotted in Figure 1.

There are as of yet very few Iridium Argo floats in the equatorial Indian Ocean, so we use 1,965 profiles from traditional and Iridium Argo floats collected from 2007 to 2014 to supplement the 1,143 shipboard CTD stations that reach at least 1990-dbar pressure collected from 1978 to 2007 within $\pm 8.5°$ latitude of the Equator (Figure 1, Table 1). We only use Argo profiles with what we deem sufficient vertical resolution. In concordance with the traditional Argo float data sampling schemes, and our stretched vertical coordinate system, we require finer vertical sampling closer to the surface. We allow no gaps >100 sdbar anywhere in the 400–1990-dbar range over which spectral analyses are applied to these profiles.

Again, there are very few Iridium Argo floats in the equatorial Atlantic Ocean, but because the Atlantic signal has the largest vertical wavelength, and because there are sufficient shipboard CTD profiles to resolve the EDJ signals in the Atlantic (Johnson and Zhang 2003), we use only those 1,312 shipboard CTD profiles from the Atlantic reaching at least 3000 dbars collected from 1972 to 2012 and containing no data gaps of greater than 20 dbars within $\pm 8.5^\circ$ latitude of the Equator (Figure 1, Table 1).

Profile processing follows Johnson and Zhang (2003). First the individual profiles are interpolated to a regular 2-dbar pressure grid, whereupon they are low-pass filtered with a 20-dbar half-width Hanning filter, and subsampled at 10-dbar intervals (Johnson et al. 2002). The profiles are then used to estimate buoyancy frequency squared, $N^2 = -(g/\rho)(\partial\rho/\partial z)$, by centered differences over 20-dbar spans where g is the acceleration due to gravity, z is depth, and ρ is the potential density referenced to a local central pressure. Linear wave theory dictates that the local vertical stratification affects the amplitudes and wavelengths of features present in the water column, so to compensate for this depth-dependent factor, Wentzel-Kramers-Brillouin-Jeffreys (WKBJ) scaling and stretching is used (Leaman and Sanford 1975). This method compensates for vertical variations in the time-average vertical stratification by stretching the vertical coordinate system and scaling the signal amplitudes. Thus, variations of vertical wavelength and amplitude of wave signatures modulated by vertical variations in the time-averaged vertical stratification are minimized, the better to identify features using standard spectral methods.

We compute approximate time- (and lateral-) average vertical profiles of N and N^2 for each basin, denoted respectively by $\langle N \rangle$ and $\langle N^2 \rangle$ as required by the WKBJ scaling (Figure 2). These quantities are computed by averaging N and N^2 at each pressure level for every profile within each basin, after which they are smoothed vertically by a 39-point (200-dbar half-width) Hanning filter (Johnson and Zhang 2003). From the filtered profiles, we compute the WKBJ scaled pressure, $p^* = (1/N_o)\int_0^p \langle N \rangle dp$, for each basin where N_o is the pressure-averaged value of $\langle N \rangle$ (Table 2) within that basin. This transformation results in the pressure range for each basin being identical in the stretched and unstretched coordinate systems. We choose the maximum depth of this range to be the zonally averaged depth of each basin along the Equator to allow estimates of the vertical mode numbers of the EDJs. However, this average depth may be less than used in other studies, so vertical mode numbers are not necessarily directly comparable.

From N^2 we compute vertical strain, $\xi_z = (N^2 - \langle N^2 \rangle)/(\langle N^2 \rangle)$, to reveal stretching and squashing of the density field. The profiles of ξ_z are first estimated on the original pressure grid, and then interpolated onto the stretched pressure grid. For this interpolation, if $\langle N \rangle > N_o$ then a simple linear interpolation is used, but if $\langle N \rangle < N_o$ then the raw values are slightly smoothed to preserve energy for vertical wavelengths of 20 sdbars and longer, due to simple linear interpolation aliasing short-wavelength information (Johnson and Zhang 2003).

We focus on the vertical range from 400–1990 dbars in the Indian and Pacific oceans and 400–3000 dbars in the Atlantic, regions where the deep jets are most apparent. While deep jets have been observed as shallow as 250 dbars, we limit the top of our range because stratification changes dramatically above 400 dbars and varies widely across basins. Previous studies have noted EDJs as deep as 3000 dbars in the Pacific and Indian oceans (e.g., Johnson et al. 2002; Dengler and Quadfasel 2002), but our range in these two oceans is limited by that of the Argo float data, which are necessary to characterize the EDJs across the entire basins using vertical strain.

3. Qualitative Description

Since the EDJs have been shown to be equatorially trapped and geostrophic (Eriksen 1982; Muench et al. 1994), their zonal velocity anomalies correspond to squashing and stretching of the density fields on the Equator, e.g. the vertical strain (ξ_z). The relationship between ξ_z and zonal velocity depends on the type of wave (Figure 3). An equatorial Kelvin wave has an on-equatorial maximum amplitude of vertical strain and velocity (Figure 3a), but a first-meridional-mode Rossby wave has an off-equatorial maximum in the vertical strain amplitude and an on-equatorial maximum velocity amplitude (Figure 3b). The maximum amplitude of ξ_z is on the Equator for Kelvin waves and off the Equator for first-meridional-mode Rossby waves (Figure 3), making it possible to use ξ_z to differentiate the two. In contrast, zonal velocity maxima are on the Equator for both waves. The main advantage of ξ_z is that density is measured much more often than velocity, allowing basin-wide analyses of ξ_z over long time-scales. Of course, there are other phenomena, such as the much shorter time-scale mixed Rossby-gravity waves, that have a signature in vertical strain fields. Those phenomena are not resolved by the CTD profiles analyzed here, and thus are treated as noise.

We discuss vertical strain contoured against pressure versus latitude, longitude, and time in the Pacific to identify the EDJs. The ξ_z profiles are smoothed by a loess filter with a half-width of 150 sdbar here, so as to reduce noise while not overly-reducing the power spectral peak at $\sim$250-sdbars vertical wavelength that will be seen in the wavelet analysis of unsmoothed profiles in Section 4. The profiles used for the meridional and zonal sections were taken between July 2013 and May 2014 to capture waves at one instance in phase of the EDJs, while averaging over the noise of high vertical mode mixed Rossby-gravity waves and other high-frequency phenonoma. Annual Rossby waves, while prominent, have vertical wavelengths of a few 1000 m (e.g., Kessler and McCreary 1993), so they are not present in the range of vertical strain vertical wavelengths analyzed here. The time period used limits the data to high-resolution Argo profiles. The contouring is done by ordinary linear interpolation.

Smoothed meridional-vertical strain at two well sampled meridians in the western and eastern Pacific Ocean (Figure 4) displays signatures of the EDJs. At both 165°E and 110°W, an off-equatorial maximum is seen at around ± 1° to ± 1.5° latitude in the sections. This off-equatorial maximum is stronger and perhaps further from the Equator at 165°E. The off-equatorial signal is also more coherent deeper in the water column, whereas the on-equatorial signal is more coherent shallower in the water column. There also appears to be a longer vertical wavelength — about 350 sdbars — for the feature at $\pm$ 1.5° latitude than for the feature on the Equator, which has a vertical wavelength of about 250 sdbars.

Smoothed zonal-vertical strain fields within 0.25° latitude of the Equator and of $\pm$1.5° latitude for July 2013 to May 2014 exhibit coherence over different zonal scales (Figure 5). Along the Equator, the vertical strain is not obviously coherent over large zonal or vertical scales. In contrast, at $\pm$1.5° latitude, the signal is visually coherent over the pressure range considered, and across the entire basin. The zonal wavelength is visually estimated to be the width of the basin, with the phase propagating downwards to the east, especially east of the dateline.

Smoothed equatorial vs. off-equatorial temporal-vertical strain fields in the eastern Equatorial Pacific (Figure 6) also have differing characteristics with a visual analysis. At the Equator, visual inspection suggests a signal in vertical strain that may be propagating upward with time with a period of about 2.5 years, but the weak coherence makes that conclusion very speculative. In contrast, at $\pm$1.5° latitude, the signal seems to propagating downward with time with a period of about 12 years over the entire pressure range. Of course, inferring a 12-year period from visual inspection of a 4-year record implies a very tentative estimate, but the signal at $\pm$1.5° latitude is much more coherent than the signal at the Equator.

In summary, there are two different latitudes in the Pacific at which there are maxima in the amplitude of the strain fields, one at the Equator and the other at around $\pm$1.5° latitude (Figure 4). The peak in the strain field at the Equator is broadly consistent with the structure of an equatorial Kelvin wave and the off-equatorial peak in the strain field is broadly consistent with an equatorial first-meridional-mode Rossby wave (Figure 4a), except for some indications of hemispheric asymmetry, which are addressed below. The equatorially-peaked feature might be propagating upwards in time with a period of 2.5 years (Figure 6a), but lacks the coherence to determine the zonal scale. The off-equatorially peaked feature seems to be propagating downward with time with a period of about 12 years and propagating downwards to the east with a zonal wavelength of the width of the basin (Figure 5,6b). Overall, the off-equatorial signal is much more coherent than the on-equatorial signal.

4. Quantitative Analysis

EDJs in the Pacific have been shown to be localized below the thermocline in the water column with a maximum amplitude near 2000 dbars (e.g., Johnson et al. 2002). Because EDJs may vary with pressure, wavelet analysis is well suited for an energy and phase analysis of the EDJs (Torrence and Compo 1998). The profiles used for wavelet analysis are not the smoothed profiles used in Section 3, but instead the interpolated profiles that should resolve signals down to a 40-sdbar vertical wavelength. The coarser sampling of the traditional Argo profiles we use in the Indian Ocean means that some of the shorter vertical wavelength energy will be lost, resolving down to 200-sdbar vertical wavelength, but with the restrictions we put on vertical gaps in the data for those profiles, they still well resolve the EDJ signals. We apply wavelet analysis over 400–2000 dbars in the Pacific and Indian oceans, and 400–3000 dbars in the Atlantic Ocean, because these are regions where $\langle N \rangle$ does not vary too much laterally, so the stretching and scaling is likely to be valid (Eriksen 1981). Since ξ_z is a normalized, prewhitened quantity, no preparation is required for the wavelet analysis (Johnson and Zhang 2003). We use a Morlet wavelet as the wavelet function, following Johnson and Zhang (2003). The profiles are zero padded to minimize edge effects and the regions where edge effects are important are blanked out. The spectra for each basin are normalized by the mean variance (σ^2) of all profiles in each basin that are located further than $\pm 3^\circ$ latitude from the Equator (Table 2). This normalization allows us to look at near-equatorial departures from an off-equatorial background level of vertical strain variance. The reduced vertical resolution of the traditional Argo profiles included in the Indian Ocean analysis may be part of the reason that σ^2 is lower there than in the other two oceans.

Mean power spectra reveal meridional and vertical structure of the EDJs (Figure 7). We analyze non-overlapping bins centered at 0°, ±0.33°, ±0.67°, ±1°, ±1.5°, ±2°, ..., ±5° latitude. In all three ocean basins, we see peaks in the power spectrum on and off the Equator (Figure 7). In both latitude ranges peaks are located near the center of the pressure range. We focus our discussions on these peaks.

In all three oceans, the equatorial peak has a slightly shorter vertical wavelength than the off-equatorial peak (Figure 7). The equatorial and off-equatorial peaks are all strongest in the Atlantic and weakest in the Pacific Ocean. The vertical wavelength of the off-equatorial peak is longest in the Atlantic and shortest in the Pacific (Figure 7, Table 2). Also, in every ocean basin there is an equatorial peak localized in the upper part of the water column (around 800 dbars) with a significantly shorter vertical wavelength than the other features. This peak may not be related to the EDJs.

The power spectra along the center of the pressure range analyzed (976 dbars Pacific, 1034 dbars Indian, 1240 dbars Atlantic) for the bins at various distances from the Equator show meridional structure of the various peaks (Figure 8). The Pacific Ocean has a very broadband peak on the Equator with a vertical wavelength of 120–400 sdbars and a much narrower peak near ±1° latitude with a vertical wavelength of 360 sdbars (Figure 8a). The Indian ocean has similar broadbanded structure near the Equator, but perhaps bracketed by distinct peaks at 120 and 400 sdbars, again with a narrow peak at 428 sdbars around ±1.5° latitude (Figure 8b). In the Atlantic, there is a very strong peak near ±1.5° latitude at a 467-sdbar vertical wavelength and a weaker peak near the Equator at 400-sdbar vertical wavelength (Figure 8c). Here we suggest that the decay of power with increasing distance from the Equator at the vertical wavelengths of the equatorial spectral peaks is consistent with the meridional structure of Kelvin waves. However, in what follows, we focus more on the off-equatorial peaks, showing that their vertical wavelength, period, and zonal wavelength are all consistent with the dispersion relation for first-meridional-mode equatorial Rossby waves in each ocean basin. Furthermore, their meridional structure, while somewhat broader than predicted by theory, otherwise agrees with it as well.

The power of ξ_z of a first-meridional-mode equatorial Rossby wave is given by $b\{[1+2(y/l)^2]\exp[-0.5(y/l)^2]\}^2$. For an equatorial Kelvin wave power is given by $d\{\exp[-0.5(y/l)^2]\}^2$. Here b is the Rossby wave energy level and d is the Kelvin wave energy level, and $l = (c/\beta)^{0.5}$ is the meridional scale, with $\beta = 2.3\times10^{-11}\mathrm{m}^{-1}\mathrm{s}^{-1}$ being the meridional derivative of the Coriolis parameter and $c = (\lambda_z N_o)/(2\pi)$ the Kelvin wave phase speed. Using the power spectra at the pressures (1049 dbar in the Pacific Ocean, 906 dbar in the Indian, and 1240 dbar in the Atlantic) and latitude bins ($\pm1°$ in the Indian and Pacific oceans, and $\pm1.5°$ in the Atlantic) with maximum off-equatorial signal in each basin, the vertical wavelengths for which the variance drops to half-maximum from the peak amplitude are used for uncertainty ranges (Table 2). This information is used to compute the likely ranges of l and vertical mode number (for the zonally averaged depth, perhaps less than the depth used in previous studies) in each ocean (Table 2).

We can further quantify the meridional structure of the EDJs by examining the power at the pressure of the maximum variance at the longer-vertical-wavelength (off-equatorial) peak in each basin (Figure 9) as a function of latitude. We use the same non-overlapping latitude bins this purpose, fitting the observed mean meridional structure of power to that predicted for equatorial Kelvin and Rossby waves of energy d and b respectively, along with a background energy level a (Figure 9). In addition to those three free parameters, we allow l, the meridional scale for the waves, to vary from the *a priori* theoretical value in each basin (Table 2). The observational estimates of l are larger by a factor of 1.5 than the theoretical values in all three basins. However, only the observational estimate of l in the Atlantic Ocean disagrees significantly with the theoretical prediction from linear wave theory when the confidence limits (given by the uncertainties in vertical wavelengths derived from the widths of the spectral peaks) are considered. At the wavelength and pressure levels analyzed in each basin, the fits again suggest that the very strong Rossby-wave signature dominates in the Atlantic Ocean, even on the Equator. In contrast, in the Indian and Pacific oceans the Kelvin wave signatures have slightly higher peak energies than the Rossby-wave signatures. Overall equatorial planetary wave energy levels are intermediate in the Indian Ocean, and lowest in the Pacific. However, even in the Indian and Pacific oceans, the Rossby-wave signature dominates the vertical strain off the Equator.

Finally, in each ocean basin we estimate periods and zonal wavelengths from observations by fitting a plane wave (e.g., $\sin(2\pi x/\lambda_x - 2\pi t/\tau + \phi)$, where the free parameters are the zonal wavelength λ_x , the period τ, and the phase offset ϕ, (see Johnson and Zhang (2003) for more information on plane wave fitting). We make these fits to phase estimates from each profile for the coherent, narrowband off-equatorial Rossby wave-like peaks in the power spectra (Table 2), again at the pressures where the peaks are a maximum in each basin (Figure 9). For each basin we carefully select an off-equatorial latitudinal band and a cut-off variance below which we do not attempt to fit the phase estimate from a profile (Figure 10). The plane waves explain only a fraction of the variance, and results are somewhat sensitive to choices of latitude bands and cut-off variances. Our selections minimize uncertainties in the fits by concentrating on phase estimates from profiles with a strong signal. Nonetheless, there is a significant spread in the phase residuals, especially in the Pacific and Indian oceans (Figure 10). In the Atlantic Ocean, the signal variance is much higher, and the fit is better. Again, the plane waves explain only a fraction of the variance in each basin, but they do show there are coherent signatures of the EDJs at basin scales and very long time periods. Furthermore, while there is sometimes asymmetry of the off-equatorial signal in quasi-synoptic sections (Figure 4), basin-wide coherent signals isolated by the plane-wave fits are indistinguishable when the analysis presented here is performed separately in each hemisphere (not shown). The coherent signals appear to be symmetric across the Equator, as expected for long Rossby waves.

The periods estimated from these plane-wave fits are 12 ± 5 years in the Pacific Ocean and 5 ± 1 years in both the Indian and Atlantic oceans (Figure 10, Table 2). The zonal wavelengths estimated from the fits are $130^\circ \pm 110^\circ$ longitude in the Pacific Ocean, $70^\circ \pm 60^\circ$ in the Indian Ocean, and $70^\circ \pm 40^\circ$ in the Atlantic Ocean. In all three oceans phase propagation for these fits is westward and downward in time, with the latter suggesting upward energy propagation if these features are indeed linear first-meridional-mode equatorial Rossby waves. While the uncertainties for the zonal wavelengths are large, their central values are on the order of the zonal width of their respective basins at the Equator. Also, given the vertical wavelength and the estimates of the period in each basin, the zonal wavelengths predicted for a first-meridional-mode equatorial Rossby wave agree very well with the central values of the observations estimates of that quantity from the plane-wave fits (Table 2). Here the theoretical zonal wavelengths are given by the linearized first-meridional-mode Rossby wave dispersion relation, $\lambda_x = \frac{c}{3}T$ where c is the Kelvin wave phase speed (Table 2). We estimate c from the observational estimate of the vertical wavelength λ_z from the spectral peak and the observational period T estimated from the planar fit. Increasing variance to the west at those wavelengths, pressures, and off-equatorial latitudes is also apparent in all three ocean basins (Figure 10).

5. Discussion

Vertical strain signatures in all three ocean basins exhibit a relatively broad-band spectral peak at the Equator over a large range of pressures below the thermocline with vertical wavelengths of a few hundred sdbar (Figure 7) and variance amplitudes significantly larger than background levels found a few degrees or more from the Equator (Figure 8). The decay in amplitude of these peaks with increasing distance from the Equator is consistent with high-vertical mode equatorial Kelvin waves (Figure 9). However, we are unable to find large-scale zonal or temporal coherence to this signal, perhaps owing to its broad-band nature caused by the superposition of Rossby and Kelvin wave signals.

In contrast, there is a narrow-band off-equatorial peak with slightly longer vertical wavelengths than the broadband equatorial peak (Figures 7, 8) in all three basins. The pattern of variance amplitude for this peak with distance from the Equator is grossly consistent with the structure of the first-meridional-mode equatorial Rossby wave, although its meridional scale is about 1.5 times wider than the theoretical scale in all three oceans (Figure 9, Table 2). These Rossby-wave-like structures exhibit large-scale zonal (Figure 5) and long-time temporal (Figure 6) coherence. Fits of a plane wave to the phase of these-off-equatorial peaks in each basin, while somewhat noisy in the Indian and Pacific oceans (Figure 10), nonetheless confirm coherent signals across the basin and over the sampling times with observational estimates of vertical wavelengths, periods, and zonal wavelengths that are completely consistent with the dispersion relation for first-meridional-mode equatorial Rossby waves (Table 2). In all three ocean basins the phase propagation for this signal is westward and downward in time, consistent with a Rossby wave and suggesting upward energy propagation if linear wave theory is applicable.

There are large differences in the variance of these signals in the different basins (Figures 7,8,9). The strongest, most coherent signal is the Rossby-wave-like one in the Atlantic Ocean, which dominates in that basin. In the Indian and Pacific oceans, the Rossby-wave-like and Kelvin-wave-like signals are of similar amplitudes, with the Pacific having the smallest amplitude signals. In addition, variance of the Rossby-wave-like signal appears to increase to the west at the pressures of maximum variance and the vertical wavelengths of the off-equatorial spectral peaks in all three ocean basins (Figure 10). Of course, given the sparse sampling in space and time in the Atlantic and Indian oceans, and the short (with respect to an estimated 12-year period) 4 years of intense sampling in the Pacific (Figure 1), it is possible that this pattern is aliased. On the other hand, it does appear in all three ocean basins.

Over the years, EDJs have been interpreted differently using linear wave theory, but the different results are not as inconsistent as they first may seem. Ponte and Luyten (1989) find two peaks in their power spectra in the equatorial Pacific Ocean, one at 560 stretched meters and the other at 331–400 stretched meters. They characterize the peak at 560 stretched meters as a first-meridional-mode Rossby wave and the peak at 331–400 stretched meters as a packet of Kelvin waves. If we adjust for different N_os used, the wavelengths of the peaks are nearly identical to those we find. Their interpretations of the different features are also almost identical to ours. The main difference is that Ponte and Luyten (1989) don't include the peak at 560 stretched meter vertical wavelength as a component of the EDJs. From Figure 4 and the analysis done in Section 3, it is clear that a component of the EDJs includes the Rossby-wave-like signal. Johnson et al. (2002) interpreted the Pacific EDJs as a Kelvin wave. However, they were only able to find a coherent phase pattern over a range of only 50° longitude in the Eastern Pacific, so their results are limited. They estimated the period to be decades long, a result which is inconsistent with the equatorial Kelvin wave dispersion relation. However, the analyses in Johnson et al. (2002) do reveal a peak in the power spectrum at a vertical wavelength longer than the Kelvin wave feature identified in the western Pacific, although they classify it as broadband noise. Thus, the signature of the Rossby wave is present even in Johnson et al. (2002), but they didn't have sufficient off-equatorial deep CTD casts to find its coherent pattern across the basin. Iridium Argo floats have remedied that situation, allowing new insights into basin-wide off-equatorial Pacific Rossby-wave like signatures in the present analysis.

Both Muench et al. (1994) in the Pacific and Johnson and Zhang (2003) in the Atlantic suggested that the observed EDJ signatures were about 1.5 times broader than their theoretical meridional scales. Our results agree with these two studies, extending that pattern to the Indian ocean. Muench et al. (1994) suggest that the presence of high-frequency motion aliases the observed meridional scale. In a modeling study Greatbatch et al. (2012) consider this widening, suggesting mixing of momentum along isopycnals as the cause. They find a widening by a factor of 1.5 over the linear theory for a realistic value of diffusion coefficient.

Johnson and Zhang (2003) analyze vertical strain data and find the EDJs in the Atlantic to be primarily first-meridional-mode Rossby waves with a period of five years, a zonal wavelength the order of the basin width on the Equator, and downward phase propagation. Analyses of velocity data by Brandt et al. (2011) results consistent with these findings. Our analysis confirms these results with a somewhat longer sampling period. In the power spectra computed in Johnson and Zhang (2003) there is also a broadband peak located at a vertical wavelength slightly shorter than the Rossby signature, although the Rossby wave peak is much more powerful. Eriksen (1982) recognizes the Kelvin wave component in vertical displacement profiles by phase relations on the Equator, but a secondary peak in energy is seen around $\pm 1.5^\circ$ latitude at 36°W, consistent with a first-meridional-mode Rossby wave.

In the Indian Ocean, a broad peak was seen by Ponte and Luyten (1990), with a range of 500–429 stretched meters. The signal at 429 stretched meters vertical wavelength was classified as a

Kelvin wave, which agrees with our analysis. The signal at 500 stretched meters was then likely the first-meridional-mode equatorial Rossby-wave-like signature that we find. The peak at 660 stretched meters vertical wavelength seen by Dengler and Quadfasel (2002) was found to be a first-meridional-mode Rossby wave, consistent with our analysis. Of course, the temporal and zonal coverage afforded by the CTD profiles allows us to make relatively robust estimates of the period and, to a lesser extent, the zonal wavelength of this signature.

It has also been suggested (e.g., d'Orgeville et al. 2007; Bunge et al. 2008; Brandt et al. 2012) that the EDJs resemble basin modes (Cane and Moore 1981), which include equatorial Kelvin and long Rossby waves with zonal wavelengths equal to the basin width. The basin mode period is equivalent to the sum of the Kelvin and Rossby wave periods, so 4/3 that of the Rossby wave alone. The zonal wavelengths on the order of the width of the basins found here in all three oceans, at least for the Rossby-wave-like signals, are quite suggestive in this regard. Also in agreement with our findings, the meridional scale of these waves is broadened by mean zonal current structure, at least in the Atlantic (Claus et al. 2014) and to a greater extent by eddy viscosity (Greatbatch et al. 2012), both of which eliminate the formation of a mid-basin caustic (Claus et al. 2014) . However, there are some aspects of the observations that are less consistent with a basin mode. Our inability to detect a coherent basin-wide equatorial Kelvin wave signal may be one discrepancy. Also, the observed variance of the off-equatorial strain at the Rossby Wave peak vertical wavelength increases to the west in all three basins (Figure 10), at odds with the signature of a simple modeled basin mode, where the Rossby Wave signature dissipates with distance from the eastern boundary (Claus et al. 2014). The observed variance at the peak vertical wavelength variance on the Equator (not shown) is fairly uniform with longitude in all three basins, where that simple modeled basin mode might exhibit variance decaying in amplitude from west to east.

The differences and similarities among the characteristics of the EDJ signatures in the three different oceans may help to narrow the possible range of plausible generation mechanisms for the EDJs. One modeling study, McCreary (1984) suggests that EDJs are superpositions of many long-wavelength Kelvin and Rossby waves, but the most visible in the model are a Kelvin wave and a first-meridional-mode Rossby wave. The deep jets have also been theorized to be generated by unstable Mixed Rossby-Gravity waves (e.g., Hua et al. 2008; Ascani et al. 2010). If that theory holds, how might it explain the differences in amplitude in the Atlantic and the other two oceans? Another theory for EDJ generation include large-vertical scale instability in western boundary currents (d'Orgeville et al. 2007). In support of this theory, the presence of stronger deep western boundary currents in the Atlantic than in the other two oceans might help explain the larger amplitude EDJ signals there. Also, the upward energy propagation observed may be consistent with this theory, since a deep energy source might imply upward energy propagation, away from that source (Brandt et al. 2011). Ascani et al. (submitted) find that deep signatures of Tropical Instability Waves in an idealized numerical Atlantic Ocean form low-frequency, baroclinic, resonant basin modes – the EDJs. Their numerical EDJ characteristics are in broad agreement with our results. However, their EDJs weaken when realistic coastlines and seasonally varying winds are included in the model.

Acknowledgments. MKY was supported by the NOAA Hollings Scholar Program, and GCJ by NOAA Research. We thank all those who helped to collect, process, calibrate, and archive the shipboard CTD and Argo data. The Argo Program is part of the Global Ocean Observing System. Argo data are collected and made freely available by the International Argo Program and the national programs that contribute to it (`http://www.argo.ucsd.edu`, `http://argo.jcommops.org`).

We also thank Francois Asçani, Eric Firing, William Kessler, Dennis Moore, LuAnne Thompson and two anonymous reviewers for useful discussions and comments.

References

Ascani, F., E. Firing, P. Dutrieux, J. P. McCreary, and A. Ishida, 2010: Deep Equatorial Ocean Circulation Induced by a Forced-Dissipated Yanai Beam*. *J. Phys. Oceanogr.*, **40 (5)**, 1118–1142.

Ascani, F., E. Firing, J. P. McCreary, P. Brandt, and R. J. Greatbatch, submitted: The deep equatorial ocean circulation in wind-forced numerical solutions. *J. Phys. Oceanogr.*

Brandt, P., A. Funk, V. Hormann, M. Dengler, R. J. Greatbatch, and J. M. Toole, 2011: Interannual atmospheric variability forced by the deep equatorial Atlantic Ocean. *Nature*, **473 (7348)**, 497–500.

Brandt, P., and Coauthors, 2012: Ventilation of the equatorial Atlantic by the equatorial deep jets. *J. Geophys. Res.*, **117 (C12)**.

Bunge, L., C. Provost, B. L. Hua, and A. Kartavtseff, 2008: Variability at intermediate depths at the equator in the Atlantic ocean in 2000-06: Annual cycle, equatorial deep jets, and intraseasonal meridional velocity fluctuations. *J. Phys. Oceanog.*, **38 (8)**, 1794–1806.

Cane, M. A., and D. W. Moore, 1981: A note on low-frequency equatorial basin modes. *J. Phys. Oceanogr.*, **11 (11)**, 1578–1584.

Claus, M., R. J. Greatbatch, and P. Brandt, 2014: Influence of the barotropic mean flow on the width and the structure of the Atlantic Equatorial Deep Jets. *J. Phys. Oceanog.*, **44 (9)**, 2485–2497.

Dengler, M., and D. Quadfasel, 2002: Equatorial Deep Jets and Abyssal Mixing in the Indian Ocean. *J. Phys. Oceanogr.*, **32 (4)**, 1165–1180.

d'Orgeville, M., B. L. Hua, and H. Sasaki, 2007: Equatorial deep jets triggered by a large vertical scale variability within the western boundary layer. *J. Mar. Res.*, **65 (1)**, 1–25.

England, M. H., and Coauthors, 2014: Recent intensification of wind-driven circulation in the Pacific and the ongoing warming hiatus. *Nature Climate Change*, **4 (3)**, 222–227.

Eriksen, C. C., 1981: Deep currents and Their Interpretation as Equatorial Waves in the Western Pacific Ocean. *J. Phys. Oceanogr.*, **11 (1)**, 48–70.

Eriksen, C. C., 1982: Geostrophic equatorial deep jets. *J. Mar. Res.*, **40**, 143–157.

Firing, E., 1987: Deep zonal currents in the central equatorial Pacific. *J. Mar. Res.*, **45 (4)**, 791–812.

Gouriou, Y., B. Bourlès, H. Mercier, and R. Chuchla, 1999: Deep jets in the equatorial Atlantic Ocean. *J. Geophys. Res.*, **104 (C9)**, 21 217–21 226.

Gouriou, Y., and Coauthors, 2001: Deep Circulation in the Equatorial Atlantic Ocean. *Geophys. Res. Lett.*, **28 (5)**, 819–822.

Greatbatch, R., P. Brandt, M. Claus, S.-H. Didwischus, and Y. Fu, 2012: On the Width of the Equatorial Deep Jets. *J. Phys. Oceanogr.*, **42 (10)**, 1729–1740.

Hua, B. L., M. D'orgeville, M. D. Fruman, C. Menesguen, R. Schopp, P. Klein, and H. Sasaki, 2008: Destabilization of mixed Rossby gravity waves and the formation of equatorial zonal jets. *J. Fluid Mech.*, **610**, 311–341.

Johnson, G. C., E. Kunze, K. E. McTaggart, and D. W. Moore, 2002: Temporal and Spatial Structure of the Equatorial Deep Jets in the Pacific Ocean. *J. Phys. Oceanogr.*, **32 (12)**, 3396–3407.

Johnson, G. C., and D. Zhang, 2003: Structure of the Atlantic Ocean Equatorial Deep Jets. *J. Phys. Oceanogr.*, **33 (3)**, 600–609.

Kessler, W. S., and J. P. McCreary, 1993: The annual wind-driven Rossby wave in the subthermocline equatorial Pacific. *J. Phys. Oceanogr.*, **23 (6)**, 1192–1207.

Leaman, K. D., and T. B. Sanford, 1975: Vertical Energy Propagation of Inertial Waves: A Vector Spectral Analysis of Velocity Profiles. *J. Geophys. Res.*, **80 (15)**.

Leetmaa, A., and P. F. Spain, 1981: Results from a Velocity Transect Along the Equator from 125 to 159 W. *J. Phys. Oceanogr.*, **11 (7)**, 1030–1033.

Luyten, J. R., and J. Swallow, 1976: Equatorial Undercurrents. *Deep-Sea Res.*, Elsevier, Vol. 23, 999–1001.

McCreary, J. P., 1984: Equatorial beams. *J. Mar. Res.*, **42 (2)**, 395–430.

Muench, J., E. Kunze, and E. Firing, 1994: The Potential Vorticity Structure of Equatorial Deep Jets. *J. Phys. Oceanogr.*, **24 (2)**, 418–428.

Ponte, R. M., and J. Luyten, 1989: Analysis and Interpretation of Deep Equatorial Currents in the Central Pacific. *J. Phys. Oceanogr.*, **19 (8)**, 1025–1038.

Ponte, R. M., and J. Luyten, 1990: Deep Velocity Measurements in the Western Equatorial Indian Ocean. *J. Phys. Oceanogr.*, **20 (1)**, 44–52.

Ropelewski, C., and P. Jones, 1987: An Extension of the Tahiti-Darwin Southern Oscillation Index. *Mon. Weather Rev.*, **115 (9)**, 2161–2165.

Schmid, C., B. Bourlès, and Y. Gouriou, 2005: Impact of the equatorial deep jets on estimates of zonal transports in the Atlantic. *Deep-Sea Res. II*, **52 (3)**, 409–428.

Torrence, C., and G. P. Compo, 1998: A Practical Guide to Wavelet Analysis. *Bull. Am. Meteorol. Soc.*, **79 (1)**, 61–78.

Weisberg, R., and A. Horigan, 1981: Low-Frequency Variability in the Equatorial Atlantic. *J. Phys. Oceanogr.*, **11 (7)**, 913–920.

LIST OF TABLES

Table 1. Summary of profile data used. 27

Table 2. Quantitative analysis parameters for and characteristics of first-meridional-mode Rossby waves in all three basins. Parameters include the depth-averaged buoyancy frequency ($N_o(s^{-1})$), the values of variance of strain (σ^2) used for normalization, the mean bottom depth along the Equator, the observed vertical wavelength (λ_z), the implied vertical mode given λ_z and the mean bottom depth, the theoretical (l–theoretical) and observationally estimated (l–fit) meridional scales, the theoretical (λ_x–theoretical) and observationally estimated (λ_x–fit) zonal wavelengths, and the observationally estimated periods of the waves. 28

TABLE 1. Summary of profile data used.

	Pacific	Indian	Atlantic
CTD	2,863	1,143	1,312
Argo	–	1,941	–
Iridium Argo	7,113	24	–
Total	9,976	3,108	1,312

TABLE 2. Quantitative analysis parameters for and characteristics of first-meridional-mode Rossby waves in all three basins. Parameters include the depth-averaged buoyancy frequency ($N_o(s^{-1})$), the values of variance of strain (σ^2) used for normalization, the mean bottom depth along the Equator, the observed vertical wavelength (λ_z), the implied vertical mode given λ_z and the mean bottom depth, the theoretical (l–theoretical) and observationally estimated (l–fit) meridional scales, the theoretical (λ_x–theoretical) and observationally estimated (λ_x–fit) zonal wavelengths, and the observationally estimated periods of the waves.

	Pacific	Indian	Atlantic
$N_o(s^{-1})$	0.0022	0.0022	0.0020
Mean variance (σ^2)	0.0885	0.0625	0.0987
Mean bottom depth (dbars)	4,050	4,200	4,100
λ_z (sdbars)	$207 < 360 < 933$	$203 < 428 < 961$	$373 < 467.5 < 635$
Vertical mode	$20 < 11 < 4$	$21 < 10 < 4$	$11 < 9 < 6$
l–theoretical	$0.51° < 0.67° < 1.08°$	$0.51° < 0.73° < 1.09°$	$0.65° < 0.73° < 0.85°$
l–fit	1.00°	1.09°	1.08°
λ_x–theoretical	144°	71°	71°
λ_x–fit	$130° \pm 110°$	$70° \pm 60°$	$70° \pm 40°$
Period–fit (years)	12 ± 5	5 ± 1	5 ± 1

LIST OF FIGURES

Fig. 1. Geographic locations of deep profiles taken since 1972 in the (a) Pacific and (c) Atlantic and Indian oceans as well as the longitude-time locations of deep profiles taken within $\pm 0.5°$ latitude of $\pm 1.5°$ in the (b) Pacific and (d) Atlantic and Indian oceans. 31

Fig. 2. Profiles of $\langle N \rangle (\mathrm{s}^{-1})$ (solid line) plotted against stretched pressure (sdbars) on the left with reference pressures (dbars) on the right for the (a) Pacific, (b) Indian, and (c) Atlantic oceans. Vertically averaged values (N_o) for each basin are also indicated (vertical dashed lines). Horizontal dotted lines bracket the vertical ranges of the vertical strain profiles used for wavelet analysis in each basin. 32

Fig. 3. Schematic of meridional structure of zonal velocity (U, dot-dashed line) and vertical strain (ξ_z, solid line) for (a) an equatorial Kelvin and (b) a first-meridional-mode equatorial Rossby wave. Each x-axis is normalized by the Kelvin wave meridional scale and y-axes shows scaled amplitudes. Figure follows Johnson and Zhang (2003) 33

Fig. 4. Meridional section of smoothed ξ_z within $\pm 2.5°$ longitude of (a) 165°E and (b) 110°W using high vertical resolution Argo CTD data taken from July 2013 to May 2014. Strain profiles are averaged in 0.5 latitude bins prior to contouring. Contour interval is 0.2 for black lines with negative values blue and positive values red. 34

Fig. 5. Zonal section of smoothed ξ_z within $\pm 0.25°$ latitude of (a) the Equator and (b) $\pm 1.5°$ latitude. Strain profiles are averaged in 3.5 longitude bins prior to contouring. Other details follow Figure 4. 35

Fig. 6. Temporal section of smoothed ξ_z within $\pm 0.6°$ latitude of (a) the Equator and (b) $\pm 1.5°$ latitude within $\pm 5°$ longitude of 110°W using high vertical resolution Argo CTD data taken from 2010 through May 2014. Strain profiles are average in 0.4 year bins prior to contouring. Other details follow Figure 4. 36

Fig. 7. Power spectra of ξ_z from all profiles (a,c,e) within $\pm 0.17°$ latitude of the Equator and (b,d,f) between $\pm 0.83°$ and $\pm 1.25°$ latitude of the Equator in the (a,b) Pacific, (c,d) Indian, and (e,f) Atlantic oceans. Contour intervals for variance are σ^2, where individual profiles have been normalized by the mean variance of profiles reaching 1990 dbars poleward of 3° latitude from the Equator in each ocean basin (Table 2). 37

Fig. 8. Average variance squared vs. vertical wavelength for various latitude bins (see legend) across the (a) Pacific, (b) Indian, and (c) Atlantic oceans. The power is taken from a depth of 976 dbars (2410 sdbars) in the Pacific, 1034 dbars (2500 sdbars) in the Indian, and 1240 dbars (2580 sdbars) in the Atlantic ocean to maximize the vertical wavelengths resolved. Vertical scales vary from smallest in the Pacific to largest in the Atlantic. 38

Fig. 9. Average power of vertical strain binned by distance from the Equator at the vertical wavelengths and pressures of the peaks around $\pm 1.5°$ latitude in Figure 8 in the (a) Pacific, (b) Indian, and (c) Atlantic oceans. Two standard errors of the mean (error bars) are used to approximate two-tailed 95% confidence intervals. Amplitudes of fitted Rossby waves (dashed lines), fitted Kelvin waves (dash-dotted lines), and the sums of the two (solid lines) are shown for each basin. 39

Fig. 10. Histograms of residuals of plane wave fits (Table 2) to phase estimates from vertical strain spectra at the pressures and vertical wavelengths used in Figures 8 and 9 for the (a) Pacific Ocean using profile with variance exceeding a 4.6 cutoff within 0.11° of $\pm 1.4°$ latitude,

(b) Indian Ocean exceeding 2.6 variance within $\pm 0.17°$ of $\pm 1.4°$ latitude, and (c) Atlantic Ocean exceeding 1.0 variance within $\pm 0.6°$ of $\pm 1.5°$ latitude. Variance for the stations (o's) within those latitude ranges plotted vs. longitude along with the three cut-off levels used (vertical dotted lines) in the (b) Pacific, (d) Indian, and (f) Atlantic oceans. 40

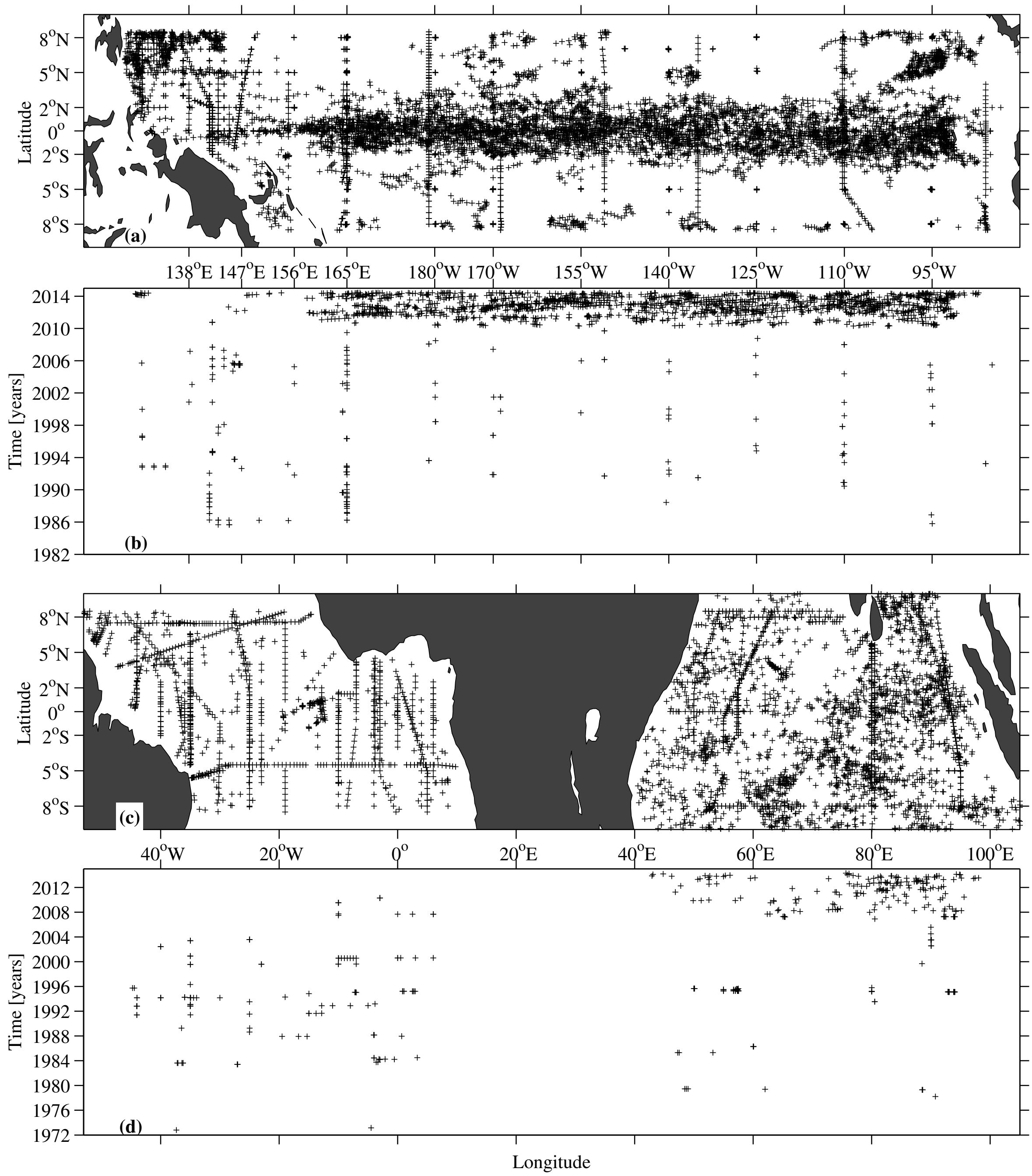

607 FIG. 1. Geographic locations of deep profiles taken since 1972 in the (a) Pacific and (c) Atlantic and Indian oceans as well as the longitude-time locations of deep profiles taken within $\pm 0.5^{\circ}$ latitude of $\pm 1.5^{\circ}$ in the (b) Pacific and (d) Atlantic and Indian oceans.

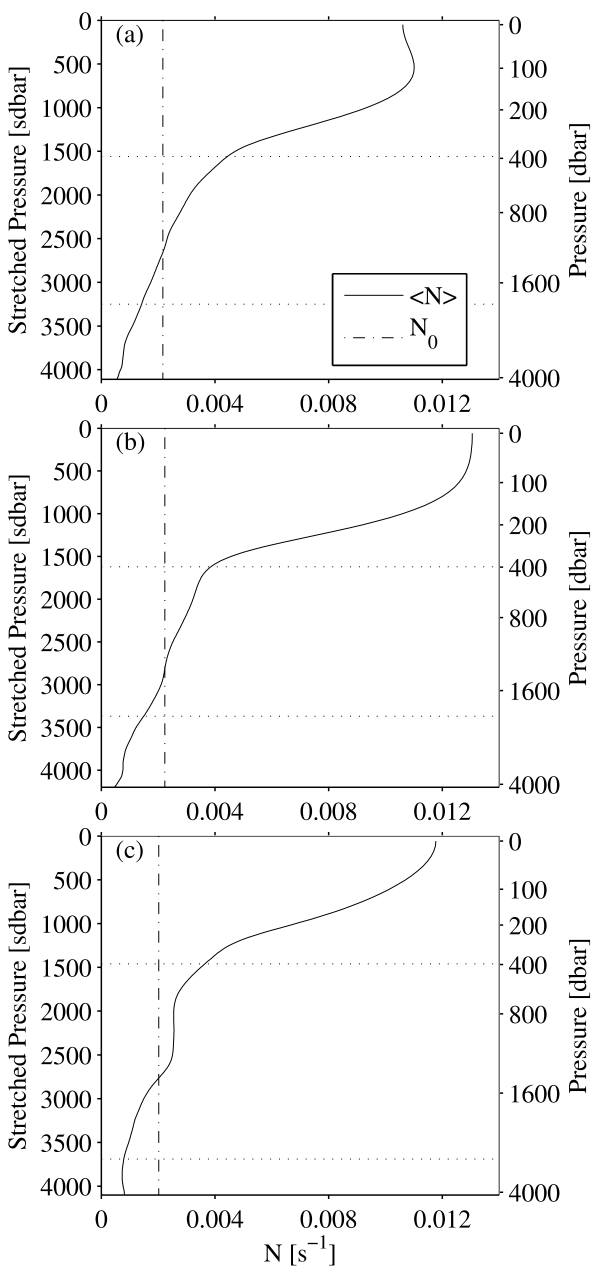

FIG. 2. Profiles of $\langle N \rangle (\mathrm{s}^{-1})$ (solid line) plotted against stretched pressure (sdbars) on the left with reference pressures (dbars) on the right for the (a) Pacific, (b) Indian, and (c) Atlantic oceans. Vertically averaged values (N_o) for each basin are also indicated (vertical dashed lines). Horizontal dotted lines bracket the vertical ranges of the vertical strain profiles used for wavelet analysis in each basin.

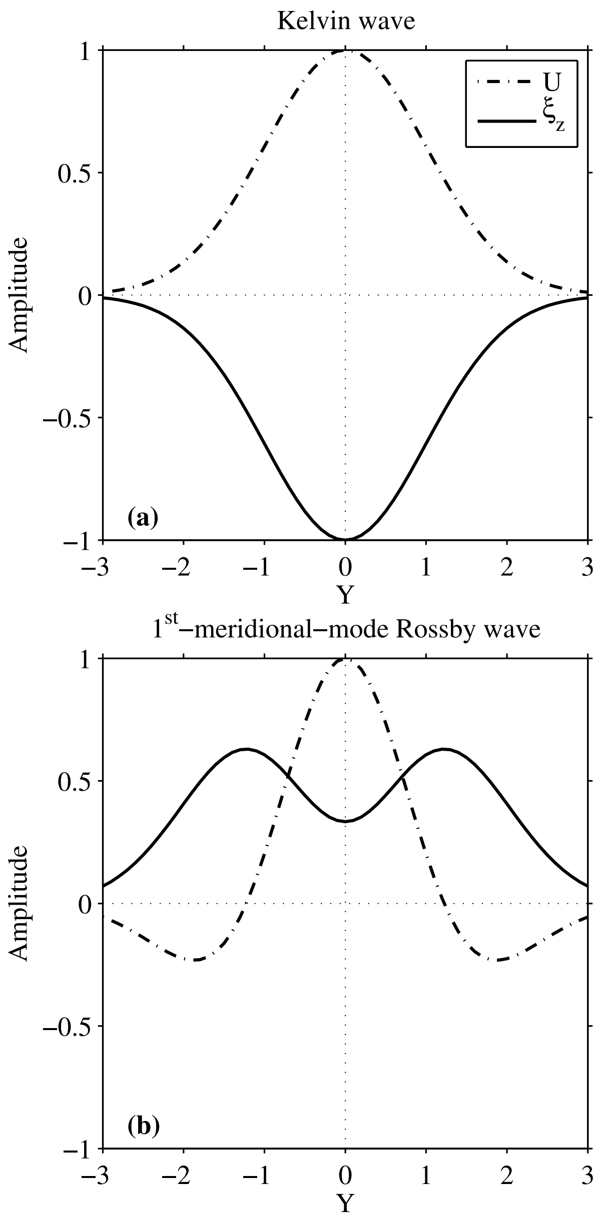

FIG. 3. Schematic of meridional structure of zonal velocity (U, dot-dashed line) and vertical strain (ξ_z, solid line) for (a) an equatorial Kelvin and (b) a first-meridional-mode equatorial Rossby wave. Each x-axis is normalized by the Kelvin wave meridional scale and y-axes shows scaled amplitudes. Figure follows Johnson and Zhang (2003)

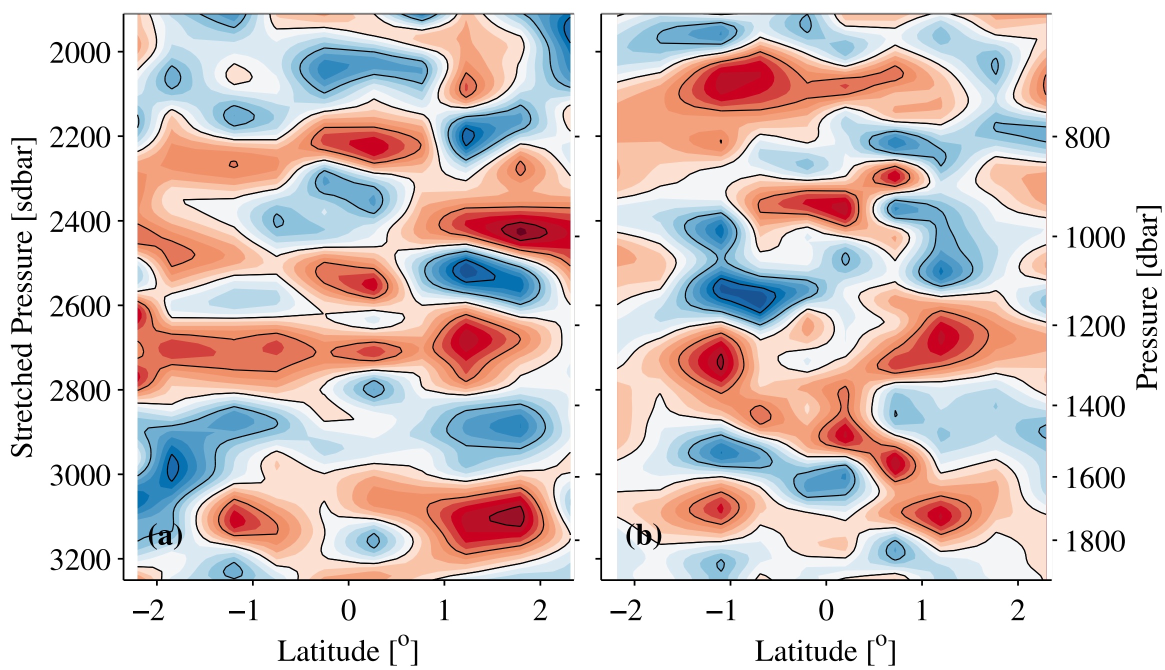

618 FIG. 4. Meridional section of smoothed ξ_z within $\pm 2.5°$ longitude of (a) 165°E and (b) 110°W using high vertical resolution Argo CTD data taken from July 2013 to May 2014. Strain profiles are averaged in 0.5 latitude bins prior to contouring. Contour interval is 0.2 for black lines with negative values blue and positive values red.

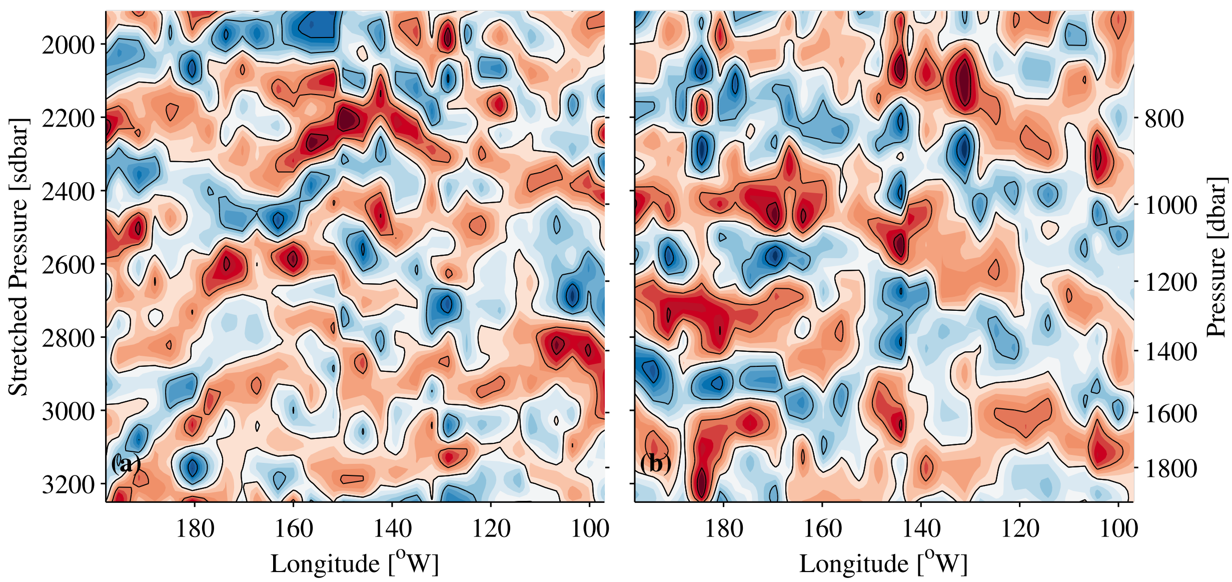

621 FIG. 5. Zonal section of smoothed ξ_z within $\pm 0.25°$ latitude of (a) the Equator and (b) $\pm 1.5°$ latitude. Strain
622 profiles are averaged in 3.5 longitude bins prior to contouring. Other details follow Figure 4.

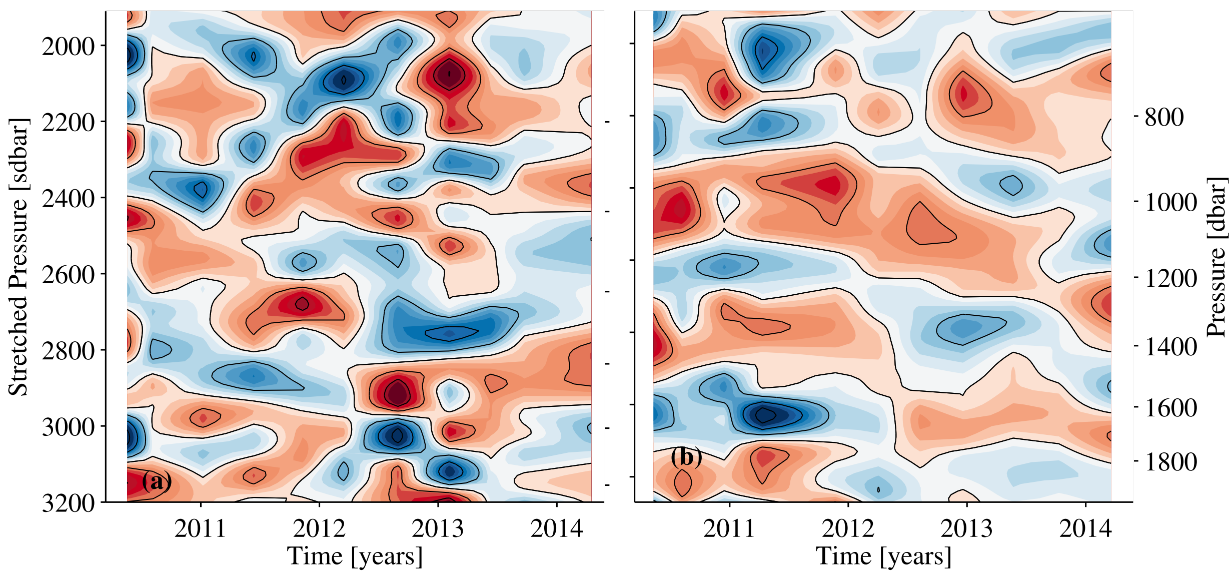

FIG. 6. Temporal section of smoothed ξ_z within $\pm 0.6°$ latitude of (a) the Equator and (b) $\pm 1.5°$ latitude within $\pm 5°$ longitude of 110°W using high vertical resolution Argo CTD data taken from 2010 through May 2014. Strain profiles are average in 0.4 year bins prior to contouring. Other details follow Figure 4.

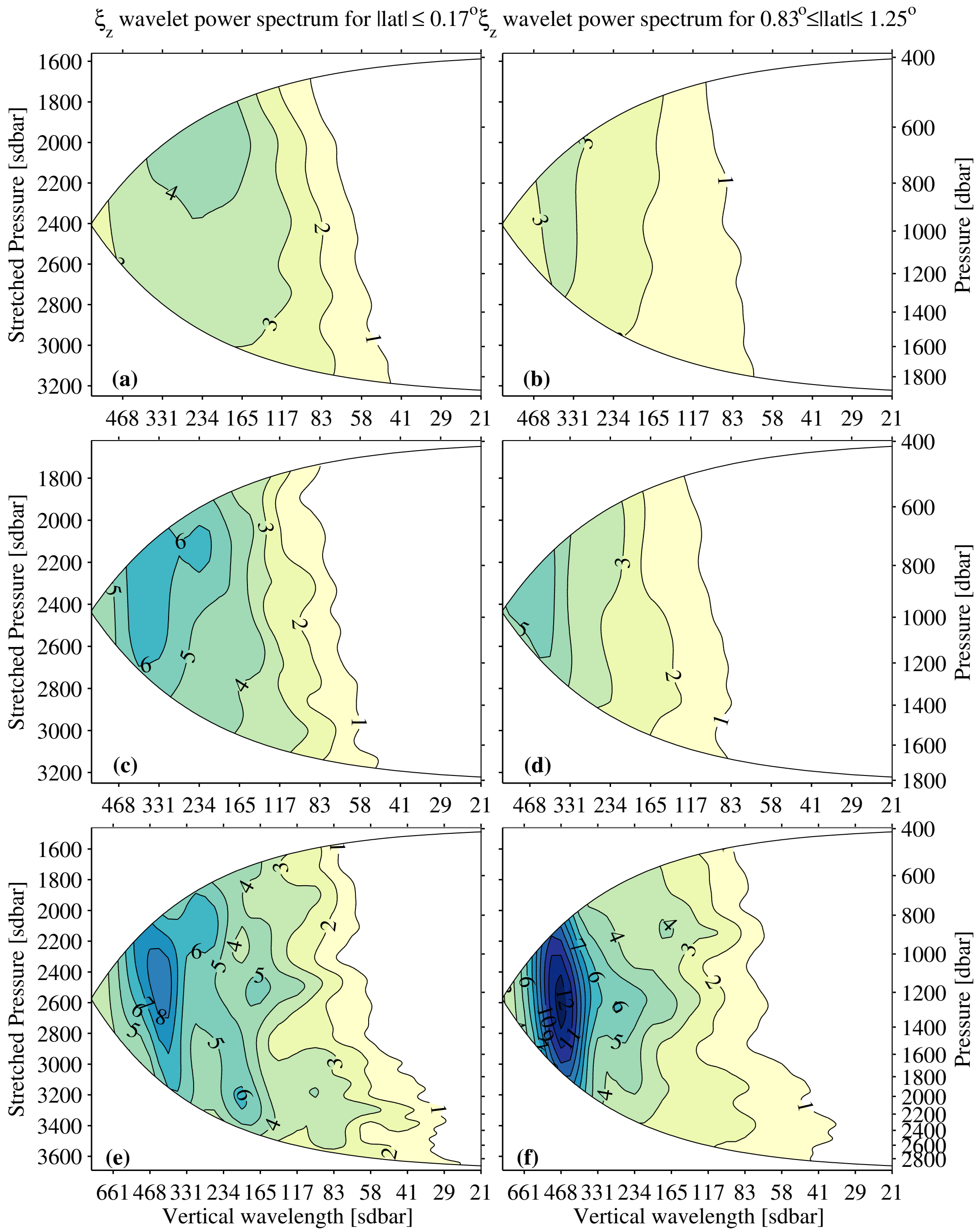

FIG. 7. Power spectra of ξ_z from all profiles (a,c,e) within $\pm 0.17°$ latitude of the Equator and (b,d,f) between $\pm 0.83°$ and $\pm 1.25°$ latitude of the Equator in the (a,b) Pacific, (c,d) Indian, and (e,f) Atlantic oceans. Contour intervals for variance are σ^2, where individual profiles have been normalized by the mean variance of profiles reaching 1990 dbars poleward of 3° latitude from the Equator in each ocean basin (Table 2).

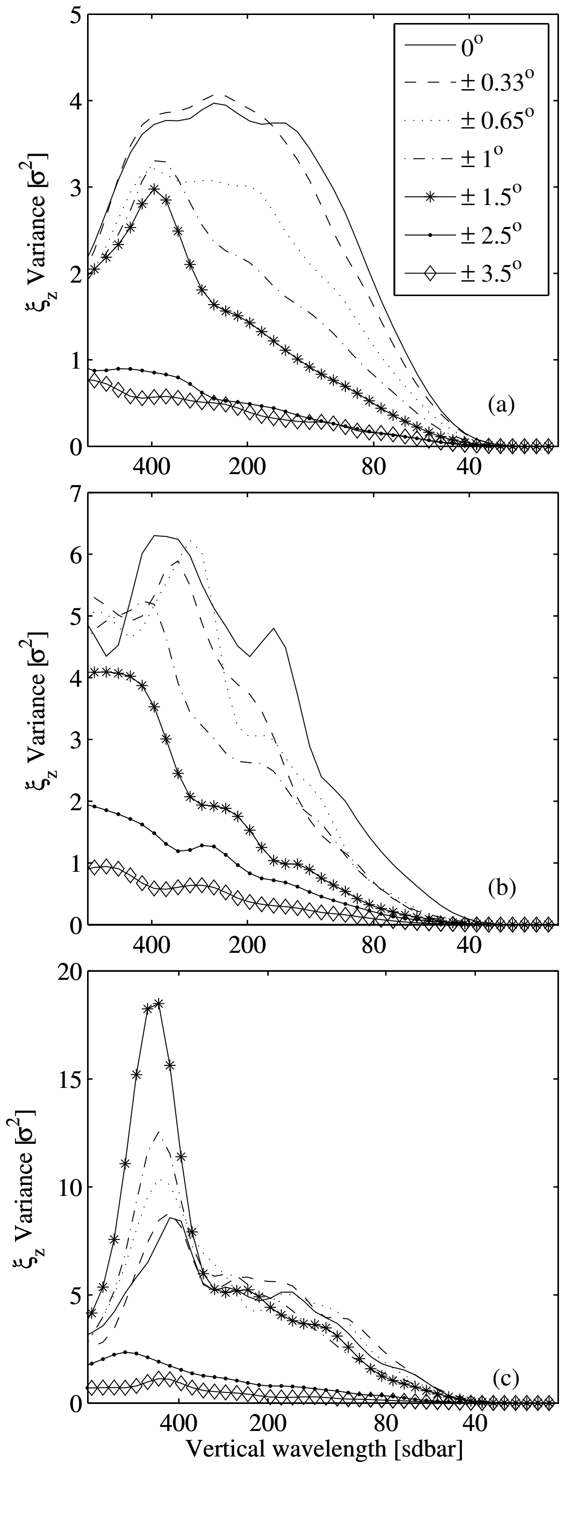

FIG. 8. Average variance squared vs. vertical wavelength for various latitude bins (see legend) across the (a) Pacific, (b) Indian, and (c) Atlantic oceans. The power is taken from a depth of 976 dbars (2410 sdbars) in the Pacific, 1034 dbars (2500 sdbars) in the Indian, and 1240 dbars (2580 sdbars) in the Atlantic ocean to maximize the vertical wavelengths resolved. Vertical scales vary from smallest in the Pacific to largest in the Atlantic.

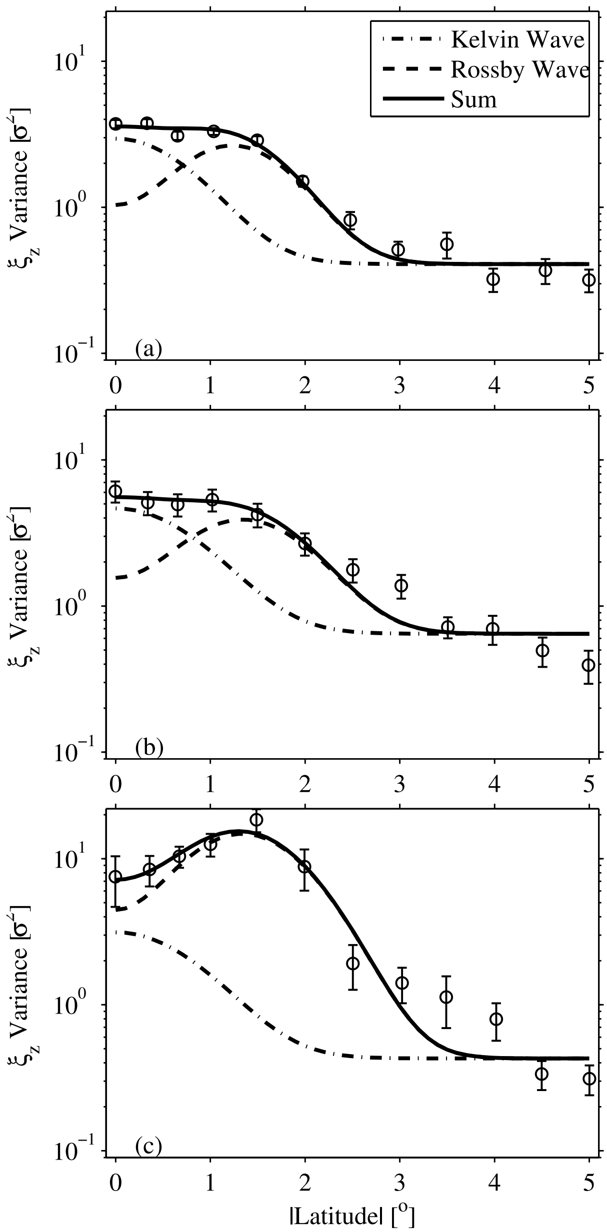

FIG. 9. Average power of vertical strain binned by distance from the Equator at the vertical wavelengths and pressures of the peaks around $\pm 1.5°$ latitude in Figure 8 in the (a) Pacific, (b) Indian, and (c) Atlantic oceans. Two standard errors of the mean (error bars) are used to approximate two-tailed 95% confidence intervals. Amplitudes of fitted Rossby waves (dashed lines), fitted Kelvin waves (dash-dotted lines), and the sums of the two (solid lines) are shown for each basin.

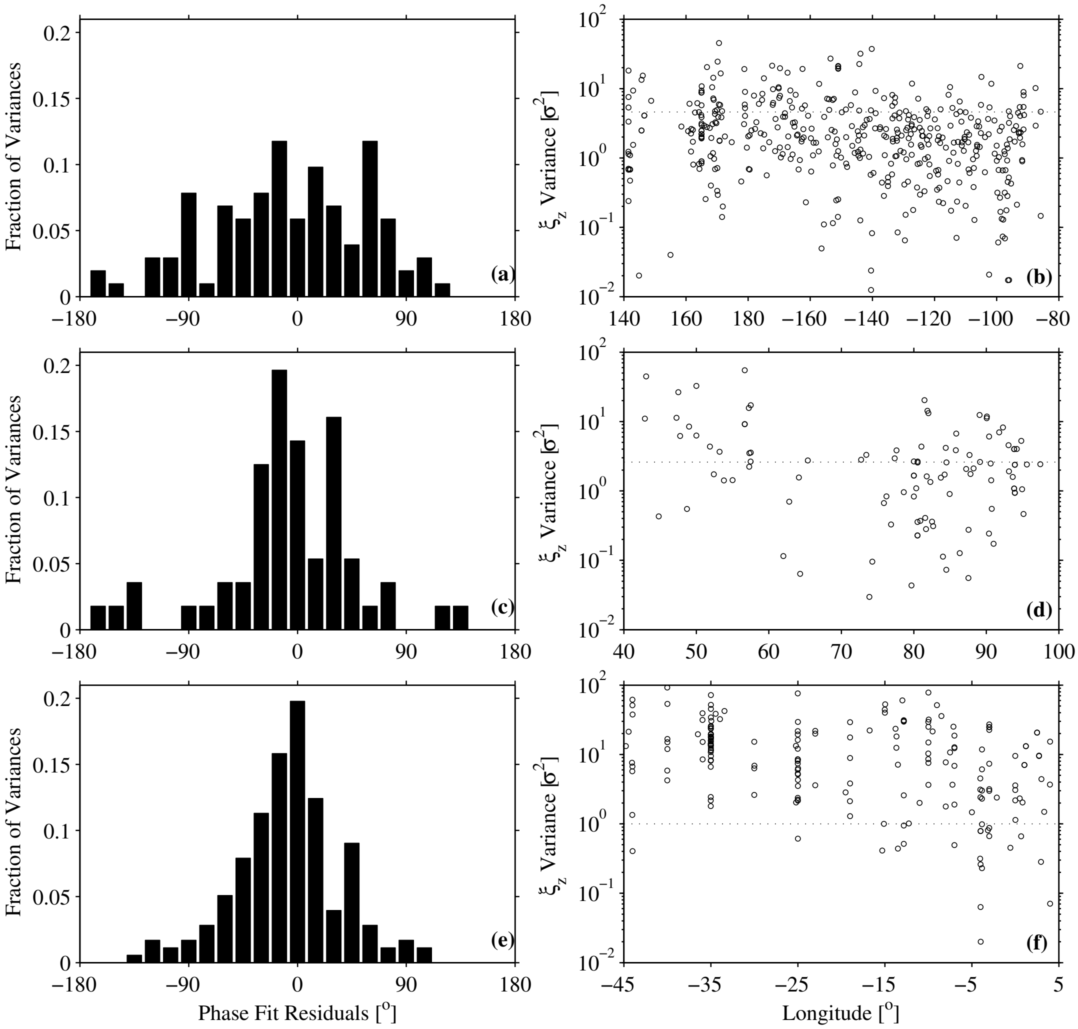

FIG. 10. Histograms of residuals of plane wave fits (Table 2) to phase estimates from vertical strain spectra at the pressures and vertical wavelengths used in Figures 8 and 9 for the (a) Pacific Ocean using profile with variance exceeding a 4.6 cutoff within 0.11° of ±1.4° latitude, (b) Indian Ocean exceeding 2.6 variance within ±0.17° of ±1.4° latitude, and (c) Atlantic Ocean exceeding 1.0 variance within ±0.6° of ±1.5° latitude. Variance for the stations (o's) within those latitude ranges plotted vs. longitude along with the three cut-off levels used (vertical dotted lines) in the (b) Pacific, (d) Indian, and (f) Atlantic oceans.